The Latitudinal Distribution of Clouds on Titan

P. Rannou, *et al.*

Science **311**, 201 (2006);
DOI: 10.1126/science.1118424

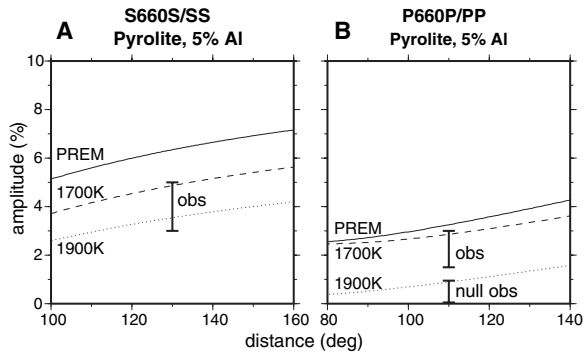

Fig. 5. Amplitudes of (**A**) *S660S*/*SS* and (**B**) *P660P*/*PP* as a function of epicentral distance range for the pyrolite model with 5% Al and mantle geotherms of 1700 K (dashed line) and 1900 K (dotted line) (*21*). The amplitudes for PREM are given for comparison (solid lines). The ranges of amplitudes found in our data are given by error bars at the average epicentral distance range, where "obs" denotes amplitudes of robust observations of *P660P* and *S660S* and "null obs" corresponds to the amplitudes when *P660P* is not observed.

PP (dotted line in Fig. 5B). Both the 1700 and 1900 geotherms also give amplitudes that fall within the range of observed amplitudes of the *SS* precursors (dashed and dotted lines in Fig. 5A). At the same time, the effect on the phase diagram of lowering Al content is identical to that of lowering the temperature. So, a lower Al content of 3% but a higher 1900 K geotherm would also lead to observable *P660P*/*PP* amplitudes (fig. S7A). We find that piclogite seismic profiles (*20*), on the other hand, cannot explain the range of amplitudes seen for *P660P*/*PP* and *S660S*/*SS* (fig. S7B).

Multiple reflectors in the depth range 660 to 720 km, or a single reflector near 720-km depth, have been explained before by multiple phase changes in garnet and ilmenite in the lower temperature regime of scenario (a) (*20*) or the end point of transformation from majorite garnet to perovskite in scenario (b). An alternative explanation for reflections from 720-km depth is possible in subduction zones. Subducted basaltic crust at the bottom of the transition zone is mainly composed of mid-oceanic ridge basalt (MORB), which has a phase transition to perovskite at 720-km depth with a positive Clapeyron slope (*23*) and could be invoked to explain some of our reflections from this depth.

Our results show a complicated seismic structure at the 660-km discontinuity, requiring lateral variations in temperature and/or minor elements such as Al in the mantle transition zone. This will influence lower mantle slab penetration and upwelling of plumes differently from region to region. Thus, the characteristics of the 660-km discontinuity and its impedance contrast can no longer be taken as a global constant when modeling mantle convection.

References and Notes

1. A. W. Hofmann, *Nature* **385**, 219 (1997).
2. G. Schubert, D. L. Turcotte, P. Olsen, *Mantle Convection in the Earth and Planets* (Cambridge University Press, Cambridge, UK, 2001).
3. A. E. Ringwood, *Composition and Petrology of the Earth's Mantle* (McGraw-Hill, New York, 1975).
4. J. Ita, L. Stixrude, *J. Geophys. Res.* **97**, 6849 (1992).
5. D. L. Anderson, *Theory of the Earth* (Blackwell Scientific, Boston, Mass., 1989).
6. P. M. Shearer, *Geophys. Monogr.* **117**, 115 (2000).
7. G. Helffrich, *Rev. Geophys.* **38**, 141 (2000).
8. S. Lebedev, S. Chevrot, R. van der Hilst, *Science* **296**, 1300 (2002).
9. E. Ito, E. Takahashi, *J. Geophys. Res.* **94**, 10637 (1989).
10. C. H. Estabrook, R. Kind, *Science* **274**, 1179 (1996).
11. P. M. Shearer, M. P. Flanagan, *Science* **285**, 1545 (1999).
12. A. Dziewonski, D. Anderson, *Phys. Earth Planet. Inter.* **25**, 297 (1981).
13. *P'P'* is shorthand for *PKPPKP*. This is an underside reflected *P* wave that travels the outer core and mantle. *PP* travels only the mantle.
14. H. M. Benz, J. E. Vidale, *Nature* **365**, 147 (1993).
15. Methods and other information available as supporting material on *Science* Online.
16. K. Chambers, J. H. Woodhouse, A. Deuss, *Earth Planet. Sci. Lett.* **235**, 610 (2005).
17. The Clapeyron slope is the slope of the transition curve in a pressure (P) versus temperature (T) phase diagram (dP/dT). These are obtained from experimental work and first-principles computer simulations. A positive (negative) Clapeyron slope corresponds in seismology with a shift to greater (lesser) depth as temperature increases.
18. J. D. Bass, D. L. Anderson, *Geophys. Res. Lett.* **11**, 237 (1984).
19. T. Irifune, A. E. Ringwood, *Earth Planet. Sci. Lett.* **86**, 365 (1987).
20. P. Vacher, A. Mocquet, C. Sotin, *Phys. Earth Planet. Inter.* **106**, 275 (1998).
21. D. J. Weidner, Y. Wang, *J. Geophys. Res.* **103**, 7431 (1998).
22. K. Hirose, *J. Geophys. Res.* **107**, 278 (2002).
23. K. Hirose, Y. Fei, Y. Ma, H.-K. Mao, *Nature* **7397**, 53 (1999).
24. N. A. Simmons, H. Gurrola, *Nature* **405**, 559 (2000).
25. K. Aki, P. Richards, *Quantitative Seismology, Vol. 1* (W. H. Freeman, San Francisco, 1980).
26. The geotherm is referenced to the temperature at a 660-km depth. For an adiabat of 1500 K (or 1600 K), which is generally assumed to be representative of average mantle temperatures, the geotherm at a 660-km depth is 1700 K (or 1850 K).
27. W. D. Mooney, G. Laske, G. Masters, *Eos* **76**, F421 (1995).
28. J. Ritsema, H. van Heijst, J. Woodhouse, *Science* **286**, 1925 (1999).

29. We thank L. Stixrude, A. de Ronde, and C. Chapman for interesting discussions. A.D. was supported by a Newly Appointed Science Lecturers Grant of the Nuffield Foundation.

9 September 2005; accepted 30 November 2005
10.1126/science.1120020

The Latitudinal Distribution of Clouds on Titan

P. Rannou,[1]* F. Montmessin,[1,2] F. Hourdin,[3] S. Lebonnois[3]

Clouds have been observed recently on Titan, through the thick haze, using near-infrared spectroscopy and images near the south pole and in temperate regions near 40°S. Recent telescope and Cassini orbiter observations are now providing an insight into cloud climatology. To study clouds, we have developed a general circulation model of Titan that includes cloud microphysics. We identify and explain the formation of several types of ethane and methane clouds, including south polar clouds and sporadic clouds in temperate regions and especially at 40° in the summer hemisphere. The locations, frequencies, and composition of these cloud types are essentially explained by the large-scale circulation.

After Voyager flybys in the early 1980s, many arguments supported the idea of condensate clouds on Titan. Because of the cold temperature at the tropopause (~70 K at altitudes of 40 to 60 km), most of the species formed in the upper atmosphere by photochemistry exceed saturation when descending. Methane, which is probably supplied at the surface, would also condense somewhere below the tropopause when transported upward. The detection of C_4N_2 ice by Voyager's IRIS (Infrared Interferometer Spectrometer and Radiometer) instrument at the north pole (*1*) constitutes the first direct evidence of condensates on Titan. Later, clouds were observed in disk-average spectra in the near-infrared (*2*, *3*) and shown lofted around 16 ± 5 km and at 27 ± 3 km. More recently, a large cloud was imaged near the south pole (*4*–*8*) at ~25 km. Cassini images (*6*, *9*) as well as recent telescope observations (*10*) also show frequent clouds scattered in the southern hemisphere at temperate mid-latitudes. These clouds are found preferentially near 40°S and are elongated in the east-west direction, forming an arc of several hundred kilometers. They are also found clustered at some preferential longitudes (*11*).

Analysis of infrared data (*12*) suggested that methane saturation ratios (the ratio between the methane partial pressure and the

[1]Service d'Aéronomie, Institut Pierre Simon Laplace, Université de Versailles-St-Quentin, BP3, 91371 Verrières le Buisson, France. [2]NASA-Ames Research Center, Moffett Field, CA 94035, USA. [3]Laboratoire de Météorologie Dynamique/IPSL, Université de Paris 6, 75252 Paris Cedex 05, France.

*To whom correspondence should be addressed. E-mail: pra@aero.jussieu.fr

methane saturation pressure) as high as 1.5 or 2 are possible. The scarcity of cloud seeds and the low wettability of aerosols by methane were invoked to justify the inhibition of the nucleation process. Several one-dimensional cloud models (*13*–*15*) predicted that the ethane and methane drops may reach diameters of several tens and hundreds of micrometers, respectively. Methane clouds could also be triggered when air parcels cool while moving from equator to pole, perhaps as a result of the quasi-barotropic motion of the atmosphere (*16*). Even with sophisticated cloud microphysics, one-dimensional models do not capture all the characteristics of the methane cycle because the vertical and sometimes the horizontal large-scale circulations are represented with simple analytical laws (*13*, *14*, *16*). The methane cycle, including condensation, has also been studied in the frame of a circulation model (*17*), but no cloud microphysics was included. Condensation was instead forced at critical saturation equal to 1 or 1.5. These models predicted that methane essentially condenses in the low troposphere, at latitudes in the ±60° range, at altitudes of 5 or 15 km, depending on the critical saturation.

To investigate the origin of clouds on Titan in a self-consistent way, we have coupled a cloud microphysical model to a general circulation model (GCM) (*18*–*21*). The results presented here follow a simulation of 25 Titan years, which is the time required to achieve a converged state. Figure 1 shows the cloud extinction along with the wind stream function at the season of Cassini arrival, two terrestrial years after the northern winter solstice. In this simulation, the haze is strongly scavenged (removed by cloud sedimentation) below 50 km at latitudes between 40°S and 40°N and around 10 km in polar regions. The scavenging produces a haze inversion layer (a zone where extinction locally increases with altitude; fig. S1) similar to that inferred from telescope data (*22*). We also identify in Figs. 1 and 2 several types of clouds: (i) widespread permanent ethane clouds, or mist, formed above the tropopause and in the troposphere everywhere in the polar regions (beyond ±60° latitude); (ii) sporadic (i.e., localized in space and time) methane clouds at altitudes between 15 and 18 km and within ±60° latitude; (iii) frequent and thick sporadic methane clouds at 15 km altitude around 40° in the summer hemisphere (south in 2005); and (iv) thick and frequent methane clouds at both poles below 30 km altitude. The physical properties that we report for these clouds match well with recent observations (Table 1).

In the stratosphere, the meridional circulation is dominated by a large pole-to-pole cell with winds ascending in the summer hemisphere and descending at the winter pole. A secondary cell, turning in the opposite direction, also exists at altitudes between 50 and 200 km in the summer hemisphere (fig. S1). The pole-to-pole cell changes direction every twelve terrestrial years (a Titan year lasts 30 terrestrial years) with a transition between two opposite cells of about three terrestrial years. The large cell downwelling branch at the winter pole is the place where chemical compounds and haze particles are brought from the stratosphere down to the troposphere (*23*, *24*). Because the tropopause is a cold point, chemical species (ethane in our model) condense on aerosols during the descent, producing a thick polar cloud everywhere below 60 km. Drops formed there are micrometer sized, smaller than but compatible with previous estimates (*14*). The related sedimentation time scale of hundreds of terrestrial days (Table 2) is long enough to maintain this cloud aloft in the polar region and to maintain a saturation ratio close to 1 (Fig. 3A). This widespread, long-lived polar cloud is rather well mixed with the winter polar haze layer (polar hood). Indirect clues for this polar cloud have been found by the Voyager IRIS, thanks to spectroscopic signatures of some condensates (*1*) or their infrared opacity (*25*). A similar process occurs at the summer pole because of the descending branch of the secondary cell, except that the aerosols and chemical species are not brought massively from the stratosphere by the descending winds, as at the winter pole. Polar haze and ethane clouds tend to increase during winter and to decrease during summer, but they persist all year round.

In the troposphere, where methane condenses, the situation is more symmetric about the equator as a result of much longer dynamical and radiative time scales. Air masses rise aslant from ~5 km near the equator to 12 km at latitude 40° in the summer hemisphere (tropics are at latitudes ±27° on Titan), then move almost vertically above 12 km and sink at high latitudes, around 60° in both hemispheres, forming two Hadley cells and an analog of the intertropical convergence zone on Earth (Fig. 1). Smaller oblique cells also appear in the polar regions, and in a stably stratified atmosphere as on Titan, these cells are triggered by strong temperature contrasts ($\Delta T \approx 5$ K) between mid-latitude regions and polar regions (fig. S2). These oblique motions occur because warm air masses move poleward into a much colder environment. They are less dense and are lifted by buoyancy along their trajectory. We find that the ascending and descending branches of these cells have a constant potential temperature below ~4 km, compatible with slantwise instabilities. In the

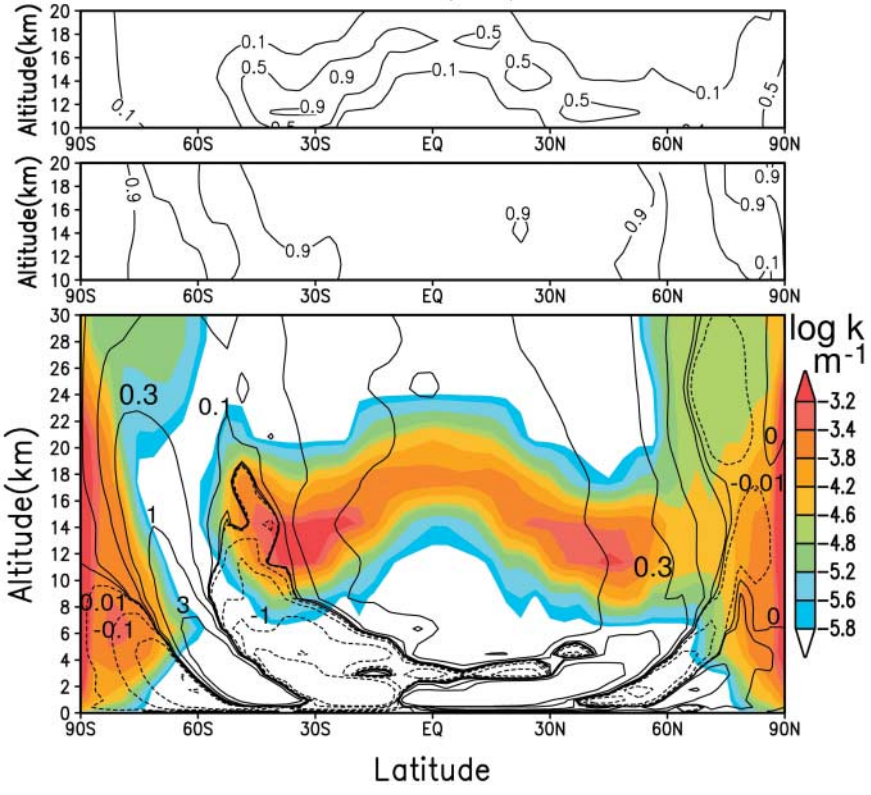

Fig. 1. (**Bottom**) Cloud extinction (m^{-1}) at 620 nm, averaged over one terrestrial year around the Cassini/Huygens arrival time, shown along with the stream function (10^9 kg s^{-1}) averaged over 7 years (one Titan season) before the arrival (continuous lines denote clockwise motion). Each result is actually the mean result of four consecutive Titan years. (**Middle**) The percentage of methane in drop composition (the remaining part is ethane). (**Top**) The fraction of time that cloud extinction exceeds a threshold of $k = 10^{-4}$ m^{-1}.

±40° latitude range, the meridional circulation has a less defined structure with uprising and downwelling motions associated with inertial instabilities. This produces vertical and horizontal mixing able to carry methane upward and to produce a broad region (between 40° in the summer hemisphere and 50° in the winter hemisphere, and below 15 km near the equator and tropics and below 12 km at the latitude edges of the region) where methane mixing ratio is almost constant (see Fig. 3B for the annual mean).

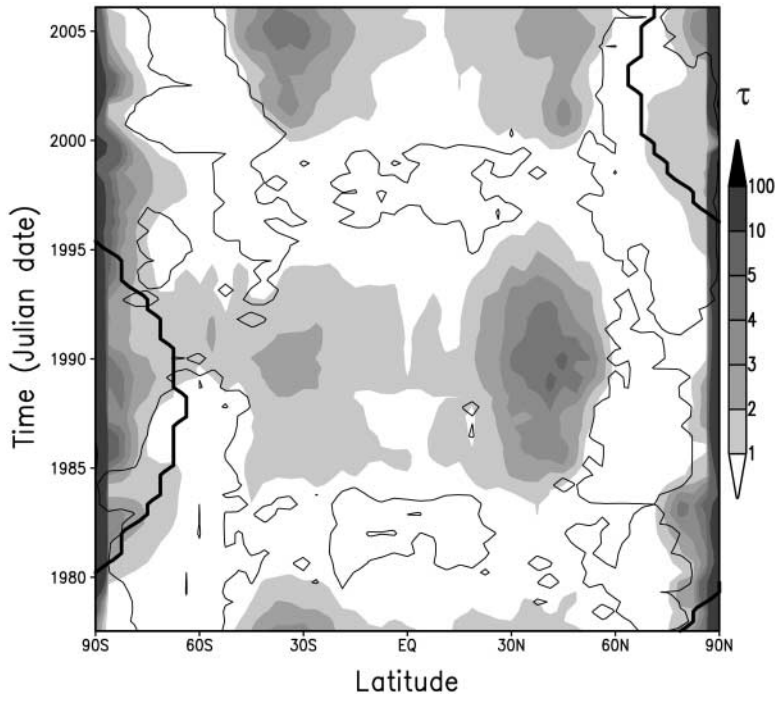

Fig. 2. Cloud column opacity (τ) at ~2 μm above 10 km altitude as a function of time and latitude. The dark thin contours show the level where 90% of the condensed material in cloud drops is methane. The thick lines show the edge of the polar night. Clouds are essentially made of methane between ±50° and near the poles, where the thick polar clouds appear. The broad cloud layer in both polar regions (poleward of latitudes ±60°) is made of ethane. Around equinoxes, during the wind cell turnover, cloud activity decreases near the equator because the aerosol concentration decreases by a factor of ~10. The summer methane polar clouds (south as observed by Cassini) tend to disappear—as observed in 2005—a few years after the summer solstice (which was in 2002) and to reappear after the following equinox (about 2010). We also expect a gradual vanishing of the summer mid-latitude clouds (at –40° in 2005) about 5 or 6 years after the summer equinox (i.e., about 2008). The mid-latitude clouds will reappear in the other hemisphere after the equinox (about 2015). These predictions should allow us to discriminate between the dynamical origin of the latitudinal cloud distribution and other possible origins, such as the location of the sources on the surface (*11*).

Methane clouds that have been observed to date appear at locations where ascending motions are predicted in our model. The observed south polar cloud (*4*–*7*, *9*) appears at the top of the oblique cells (exactly at the south pole, at altitudes of 20 to 30 km). The large recurrent zonal (longitudinal direction) clouds at 40°S (*9*–*11*), as well as the linear and discrete clouds found at several locations between 14°S and 83°S and clustered at 40°S (*6*), are correlated with the ascending branch of the tropospheric Hadley cell (at 40°S in 2005) and to the broad region where vertical mixing occurs (Fig. 1). Consistently, our model produces clouds at the places where clouds are actually observed (Table 1), but it also predicts clouds that have not (or not yet) been observed. Generally, in our model, methane condenses at ~15 km at ±60° latitude and at 18 km near the equator. Clouds are formed at these levels anywhere methane is transported upward by the circulation (Fig. 1). Methane clouds frequently appear in the ascending branch of the tropospheric Hadley cell at ~40° in the summer hemisphere (south in 2005). The mixing process due to inertial instabilities also produces thin clouds between ±30° (about 10% of the time) and more important clouds (between 10 and 50% of the time) at winter mid-latitudes (between 40° and 60°), although wind is descending there (Fig. 2). The mixing process produces a broad region (from 30° in the summer hemisphere to 60° in the winter hemisphere and below ~10 km; Fig. 3B shows the annual mean value) where the methane ratio is almost uniform and close to 5% (which is about the surface value in the ±30° range). Between tropics, the warm temperatures and the presence of clouds bound the saturation ratio close to 1, consistent with Huygens observations (*26*). Between 40° and 60° winter latitudes, temperature sharply decreases with latitude (fig.

Table 1. Cloud classification.

Cloud type	Location/origin	Optical thickness	Drop radius (μm)	Lifetime	Related observations
Ethane mist	Both polar regions below 60 km / Descending branch of stratosphere cells	~1 to 5	1 to 3	Permanent structure	C_4N_2 detected at winter pole (*1*); cloud opacity (*25*); summer pole not yet observed
Polar methane	Poleward 75° at both poles and below 30 km / Slantwise cells between mid-latitudes and poles	~10 to 100	10 to 100	Terrestrial day	5 to 25 km, scattered in south (summer) polar region (*4*, *6*–*8*); north (winter) pole not observed yet
Sporadic tropical methane	~40° in summer hemisphere at or below 20 km / Ascending branch of the troposphere Hadley cell	~1 to 100	10 to 100	Terrestrial day	5 to 7% of the disk*, time scale = 2 days (*2*, *3*); discrete and streak clouds clustered around 40°S (*6*, *9*–*11*) and between 63°S and 83°S (*6*)
Sporadic intertropical methane	Between ±30° at or below 20 km / Mixing process due to inertial instabilities	~1 to 100	10 to 100	Hour	0.5% of the disk*, time scale = hours (*3*); streak cloud at 14°S, 23°S (*6*); not observed in north (winter) hemisphere

*Data used by (*2*, *3*) are disk-integrated near-infrared spectra; determination of cloud location thus strongly depends on hypothesis, and clouds may actually be elsewhere than near the equator.

S2), producing a permanent zone of supersaturation (Fig. 3A) in the regions depleted in aerosols (fig. S1). This pocket of supersaturation is fed by mixing, and clouds that form at the lower edge of the aerosol-depleted region do not efficiently remove the excess methane. These conditions are favorable to form frequent winter mid-latitude clouds.

With radii of ~30 to 100 μm, methane drops rapidly settle and evaporate a few kilometers lower, in subsaturated layers. The sedimentation time scale is much smaller than the time scale to restore, by mixing or upward advection, the methane saturation ratio up to the critical saturation ratio (the ratio at which nucleation is triggered, predicted to be $S \approx 1.02$ in our model with our parameter set; table S1). Therefore, methane clouds essentially appear as sporadic clouds rather than as a permanent cloud deck. Their lifetime is limited by their sedimentation time scale (several terrestrial days), but small clouds have very short lifetimes due to a shorter evaporation time scale (hours) (Table 2).

Table 2. Average time scales in Titan atmosphere.

Physical process	Polar region	Tropical regions
Cloud microphysics	Hour*	Hour*
Ethane cloud sedimentation†	Terrestrial year	
Sporadic methane cloud sedimentation†	Day to week	Day to week
Aerosol sedimentation†	Decades to century	Decades to century
Horizontal meridional wind‡	Century	Decades to century
Horizontal zonal wind§	Terrestrial day	Terrestrial day
Vertical wind‖	Century	Century
Vertical mixing processes¶		Decades#

*Relaxation time from situations out of equilibrium. †Scale height H divided by sedimentation speed. ‡For latitudinal motions: Titan radius R divided by latitudinal wind speed v. §For zonal (longitudinal) motions: Titan perimeter $2\pi R$ divided by zonal wind speed u. ‖Mixing due to inertial instabilities between ±60°. ¶For vertical motions: Scale height H divided by vertical wind speed w. #Roughly estimated from situations out of equilibrium.

The zonal wind speed—several tens of meters per second—exceeds the speed of the two other wind components, and it has a vertical gradient (U_z') of ~0.5 m s^{-1} km^{-1} between the ground and ~20 km (*27*). This may explain why tropospheric clouds at mid-latitudes, which have vertical extents of a few kilometers, appear elongated in the zonal direction. Dimensions L of several hundred kilometers ($L \approx \Delta U \times \Delta t \approx 2 \times 10^5$ m) are explained by the differential zonal speed inside the cloud ($\Delta U \approx U_z' \times \Delta z \approx 2.5$ m s^{-1}) due to their vertical extent ($\Delta z \approx 5$ km) and their formation lifetime (one terrestrial day: $\Delta t \approx 10^5$ s). At both poles, cloud structures are also produced by the oblique cells that carry methane-rich air upward from the surface at ±40° latitudes to higher altitudes in polar regions, where it condenses. Very near the poles, the cells have a strong vertical component that produces clouds at the same place as those observed (*6*). The methane polar cloud is pinned very near the poles. It is variable in time and space and also has a variable vertical extent that may occasionally reach up to 30 km. In our model, the air is very stable, the latent heat is negligible, and therefore no convection can produce the polar clouds with the mechanism proposed in (*4*).

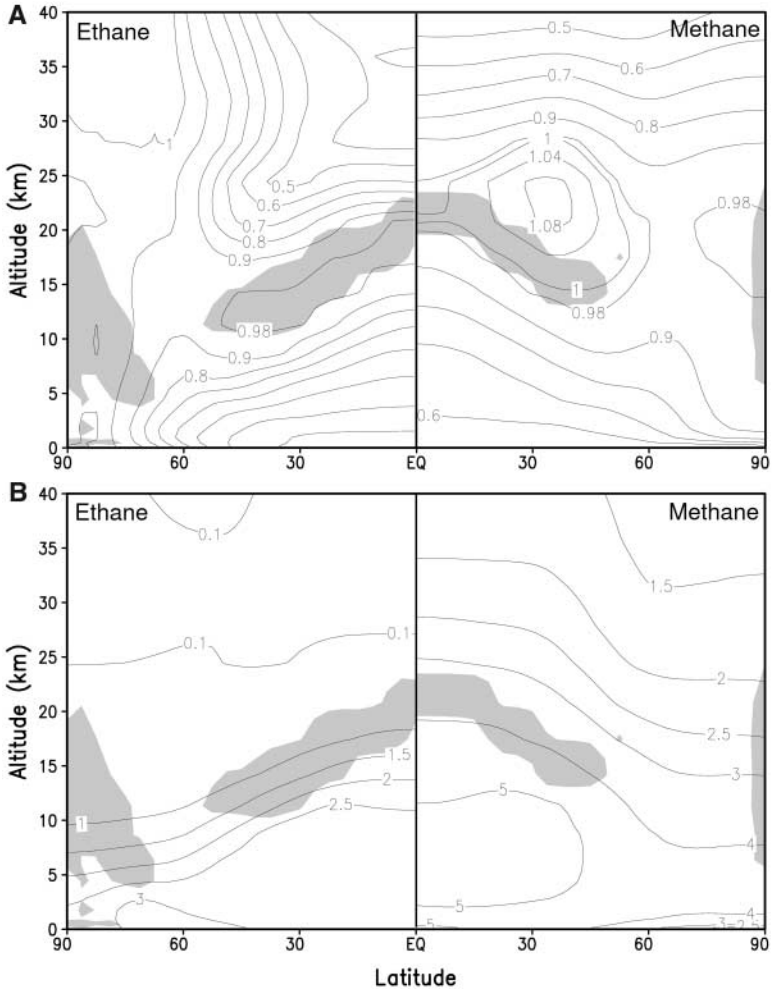

Fig. 3. (**A**) Annual mean of ethane (left) and methane (right) saturation ratios. Here we find that high saturation levels are tightly correlated to cloudy regions (Fig. 1). The shaded areas show places where ethane and methane annual condensation rates are larger than threshold values of 10^{-21} and 6×10^{-17} m^3 of ice per m^3 of atmosphere per second, respectively. On the left, ethane condenses below 60 km in the polar regions and then evaporates during the descent. This allows maintenance of the ethane concentration close to saturation down to the surface in the polar regions. Lower troposphere circulation and mixing processes transport ethane-humid air from the poles to warmer undersaturated tropical regions, where air masses rise up and cool leading ethane close to saturation again around 15 km or 18 km. On the right, a similar process is at work for methane, except that the source is at the surface. Rising motions in the tropics and in both polar regions generate a layer where methane saturation is close to 1 at ~20 km near the equator, at 15 km at mid-latitudes, and between 10 and 20 km at the poles. Methane saturation ratio sharply drops above 25 km. Methane annual mean saturation ratio close to 1 at 12° is more consistent with Huygens observations (*26*) than with previous estimations from Voyager IRIS data (*30*). (**B**) Ethane and methane mixing ratios. Both species are rather constant in the first 10 km and within ±40°. Shaded areas have the same meaning as in the upper panel.

Ethane precipitation occurs essentially in large regions poleward of ±70°, with ~0.2 mm per Titan year in polar regions and a few micrometers per year elsewhere. The methane cycle is a balance between the surface evaporation and precipitation. Methane evaporates between the tropics (in the ±30° range) and precipitates near the poles. In tropical regions, most of the methane clouds evaporate before reaching the ground, except for the largest ones. At latitudes of ±70°, methane precipitation does not exceed 1 cm per year, but poleward of ±70° it can reach 1 m per year. The global cycle then drives methane from equatorial and tropical to polar regions. Methane is probably not stable in tropical regions on geological time scales, and because the Huygens landing site was humid and marked by river channels, this indicates that a source of methane is still active on Titan (*28*). Global average values of precipitation rates found here are consistent with previous work (*14*, *17*).

The methane cycle on Titan has some similarities with water cycles on Earth and on Mars. As with water on Earth and Mars, the methane source on Titan is at the surface. The major cloud pattern on these planets essentially appears in ascending branches of the circulation: (i) The Hadley cell system produces a cloud belt in the intertropical convergence zone on Earth and on Mars and also produces the frequent clouds at 40° in the summer hemisphere on Titan. (ii) The poleward ascending motions beyond the Hadley cell, developed as baroclinic waves on Earth and on Mars and as slantwise convection in our two-dimensional model of Titan, produces clouds because water or methane-rich air is transported toward cold regions. This mechanism produces the south polar cloud. Baroclinic waves are believed not to be produced on Titan (*17*). In these three atmospheres, clouds are generally good tracers of the circulation and can reveal some of its important features.

Gravitational tides caused by Saturn are known to disturb the large-scale circulation (*29*). This effect is specific to Titan and could explain the longitudinal large-scale distribution of the clouds (*11*) by triggering nucleation at preferential longitudes. Surface heterogeneities (albedo contrasts and topography) and waves may also play a role in circulation and in cloud meteorology. These questions must be addressed further, in the frame of a three-dimensional model.

Some cloud properties may be defined, in reality, at scales smaller than the model grid [e.g., cloud overshoots, subscale inhomogeneities as observed by (*9*)]. Interaction between clouds and haze in our model may also lead to removal of aerosols more efficiently than observed in reality (*27*). Clouds in our circulation model are necessarily simplified relative to the real clouds. However, the main cloud features predicted in this work find a counterpart in reality. The correct behavior of our model allows us to analyze the formation mechanism associated with each type of observed cloud and offers a new insight into cloud physics on Titan.

References and Notes

1. R. E. Samuelson, L. A. Mayo, M. A. Knuckles, R. J. Khanna, *Planet. Space Sci.* **45**, 941 (1997).
2. C. A. Griffith, T. Owen, G. A. Miller, T. Geballe, *Nature* **395**, 575 (1998).
3. C. A. Griffith, J. L. Hall, T. R. Geballe, *Science* **290**, 509 (2000).
4. M. E. Brown, A. H. Bouchez, C. A. Griffith, *Nature* **420**, 795 (2002).
5. S. G. Gibbard *et al.*, *Icarus* **169**, 429 (2004).
6. C. C. Porco *et al.*, *Nature* **434**, 159 (2005).
7. H. G. Roe, I. De Pater, B. A. Macintosh, C. P. McKay, *Astron. J.* **591**, 1399 (2002).
8. A. H. Bouchez, M. E. Brown, *Astron. J.* **618**, L53 (2005).
9. C. A. Griffith *et al.*, *Science* **310**, 474 (2005).
10. H. G. Roe, A. H. Bouchez, C. A. Trujillo, E. L. Schaller, M. E. Brown, *Astron. J.* **618**, L49 (2005).
11. H. G. Roe, M. E. Brown, E. L. Schaller, A. H. Bouchez, C. A. Trujillo, *Science* **310**, 477 (2005).
12. R. Courtin, D. Gautier, C. P. McKay, *Icarus* **114**, 144 (1995).
13. R. E. Samuelson, L. A. Mayo, *Planet. Space Sci.* **45**, 949 (1997).
14. E. L. Barth, O. B. Toon, *Icarus* **162**, 94 (2004).
15. R. D. Lorenz, *Planet. Space Sci.* **41**, 647 (1993).
16. E. L. Barth, O. B. Toon, *Geophys. Res. Lett.* **31**, L17S07 (2005).
17. T. Tokano, F. M. Neubauer, M. Laube, C. P. McKay, *Icarus* **153**, 130 (2001).
18. F. Hourdin *et al.*, *Icarus* **117**, 358 (1995).
19. P. Rannou, F. Hourdin, C. P. McKay, *Nature* **418**, 853 (2002).
20. P. Rannou, F. Hourdin, C. P. McKay, D. Luz, *Icarus* **170**, 443 (2004).
21. See supporting material on *Science* Online.
22. E. F. Young, P. Rannou, C. P. McKay, C. A. Griffith, K. Noll, *Astron. J.* **123**, 3473 (2002).
23. S. Lebonnois, D. Toublanc, F. Hourdin, P. Rannou, *Icarus* **152**, 384 (2001).
24. F. Hourdin, S. Lebonnois, D. Luz, P. Rannou, *J. Geophys. Res.* **109**, E10005 (2004).
25. L. A. Mayo, R. E. Samuelson, *Icarus* **176**, 316 (2005).
26. H. B. Niemann *et al.*, *Nature* **438**, 779 (2005).
27. M. Tomasko *et al.*, *Nature* **438**, 765 (2005).
28. C. Sotin *et al.*, *Nature* **435**, 786 (2005).
29. T. Tokano, F. M. Neubauer, *Icarus* **158**, 499 (2002).
30. R. E. Samuelson, N. R. Nath, A. Borysow, *Planet. Space Sci.* **45**, 959 (1997).

31. Supported by the Programme National de Planétologie du CNRS. This work was performed while F.M. held a tenure from the National Research Council associateship program.

Supporting Online Material

www.sciencemag.org/cgi/content/full/311/5758/201/DC1
Materials and Methods
Figs. S1 and S2
Table S1
References

4 August 2005; accepted 9 November 2005
10.1126/science.1118424

Majority Logic Gate for Magnetic Quantum-Dot Cellular Automata

A. Imre,[1]* G. Csaba,[2] L. Ji,[1] A. Orlov,[1] G. H. Bernstein,[1] W. Porod[1]

We describe the operation of, and demonstrate logic functionality in, networks of physically coupled, nanometer-scale magnets designed for digital computation in magnetic quantum-dot cellular automata (MQCA) systems. MQCA offer low power dissipation and high integration density of functional elements and operate at room temperature. The basic MQCA logic gate, that is, the three-input majority logic gate, is demonstrated.

In magnetic devices, information is encoded in the magnetization state of ferromagnetic materials. Although commonly used for data-storage applications, there are relatively few attempts to exploit magnetic phenomena for logic functionality (*1*–*5*). One of the possible architectures suitable for logic using nanomagnets is the quantum-dot cellular atomata (QCA) signal-processing approach (*6*). QCA are built from simple, (nominally) identical, bistable units that are locally connected to each other solely by electromagnetic forces; consequently, the signal-processing function is defined by the physical placement of the building blocks that constitute the computing architecture (*7*–*9*). Recently, Cowburn and Welland (*2*) described the realization of magnetic QCA (MQCA) operation in chains of 110-nm-diameter disk-shaped magnetic particles that manifest collective behavior. In this system, the preferred magnetization direction of the disks (the representation of binary information), as well as the magnetization reversal process (the information propagation), is primarily determined by coupling-induced magnetic anisotropy in the chains. Our approach to MQCA is similar in spirit, but we use an additional shape-induced anisotropy component to separate the directions for magnetic information representation and information propagation in the array (*5*).

The QCA concept can be realized in different physical systems. It was originally proposed to use electrostatically coupled arrays of quantum dots and Coulomb-blockade phenomena to perform binary operations (*6*). The

[1]Center for Nano Science and Technology, Department of Electrical Engineering, University of Notre Dame, Notre Dame, IN 46556, USA. [2]Institute for Nanoelectronics, Technical University of Munich, Arcisstrasse 21, D-80333 Munich, Germany.

*To whom correspondence should be addressed. E-mail: aimre@nd.edu